Polarimetric passive microwave remote sensing of wind vectors with foam-covered rough ocean surfaces

Lin Zhou and Leung Tsang[1]

Department of Electrical Engineering, University of Washington, Seattle, Washington, USA

Dong Chen

Department of Electronic Engineering, City University of Hong Kong, Kowloon, Hong Kong

[1] In this paper, polarimetric microwave emissions from wind-generated foam-covered ocean surfaces are investigated. The foam is treated as densely packed air bubbles coated with thin seawater coating. The absorption, scattering and extinction coefficients are calculated by Monte Carlo simulations of solutions of Maxwell equations of a collection of coated particles. The effects of boundary roughness of ocean surface are included by using the second-order small perturbation method (SPM) describing the reflection coefficients between foam and ocean. An empirical wavenumber spectrum is used to represent the small-scale wind-generated sea surfaces. The iterative method is employed to solve dense media radiative transfer (DMRT) equations, and is applied to calculate results of all four Stokes parameters of rough ocean surfaces. The theoretical results of four Stokes brightness temperatures with typical parameters of foam in passive remote sensing at 10.8 *GHz*, 19 *GHz* and 36.5 *GHz* are illustrated. The azimuth variations of polarimetric brightness temperature are calculated. Emission with various wind speed and foam layer thickness is studied. The results are also compared with those based on Quasi-Crystalline Approximation (QCA). *INDEX TERMS:* 6969 Radio Science: Remote sensing; 0689 Electromagnetics: Wave propagation (4275); 0659 Electromagnetics: Random media and rough surfaces; *KEYWORDS:* dense media radiative transfer, four strokes parameters, ocean foam

1. Introduction

[2] Fully polarimetric microwave remote sensing means that all four Stokes parameters are measured [*Tsang*, 1991]. There has been an increasing interest in the applications of polarimetric microwave radiometers for ocean wind remote sensing [*Yueh et al.*, 1994; *Johnson et al.*, 1994; *Yueh*, 1997; *Kunkee and Gasiewski*, 1997]. It is known that foam on the ocean surface can affect the brightness temperatures measured by microwave radiometers. Although foam typically cover only a few percent of sea surfaces, increasing foam coverage on the sea surface can substantially increase the

sea surface emissivity [*Stogryn*, 1972; *Smith*, 1988; *Huang and Jin*, 1995]. However, there is relatively little known definitively concerning the impact of foam on the retrieval of the ocean surface wind vector from satellite-mounted microwave instruments. This gap in knowledge is due in large part to the difficulty in making measurements at high wind speeds, when significant foam coverage is present. In the past, empirical microwave emissivity models [*Stogryn*, 1972; *Smith*, 1988; *Williams*, 1971; *Wilheit*, 1979; *Pandey and Kakar*, 1982; *Yueh*, 1997] were used to estimate the effect of the foam above the ocean surface on the passive microwave remote sensing measurements. These are empirical fitting procedures using experimental data. Recently, a physically based approach taking into account the microstructure of foam was developed [*Guo et al.*, 2001; *Chen et al.*, 2003]. The model treats the foam as densely packed air bubbles coated with thin seawater coating. It was

---

[1]Also at Department of Electronic Engineering, City University of Hong Kong, Kowloon, Hong Kong.

shown that the polarization and frequency of the brightness temperatures depend on the physical micro-structure properties of foam and the foam layer thick-ness. *Guo et al.* [2001] used the Quasi-Crystalline Approximation (QCA) model for foam, while *Chen et al.* [2003] used the Monte Carlo Simulations. Controlled experiments of radiometric measurements of foam microwave emissions have also been made [*Rose et al.*, 2003].

[3] In this paper, the polarimetric microwave emis-sions from wind-generated foam-covered rough ocean surfaces are studied. The dense media model of foam is applied to calculate the values of the complex effective propagation constants, the extinction coefficients and the albedo. These are used to describe the character-istics of the foam layer. The effects of boundary rough-ness of ocean surface are included in the boundary conditions of DMRT by using the second-order small perturbation method (SPM) [*Tsang et al.*, 1985; *Yueh et al.*, 1994; *Tsang and Kong*, 2001] describing the bistatic reflection coefficients between foam and ocean. The small-scale wind-generated sea surfaces are generated by using an empirical wavenumber spectrum [*Durden and Vesecky*, 1985]. The iterative method is employed to solve dense media radiative transfer (DMRT) equations. The method is summarized in Section 2. The parameters of foam model are described in Section 3. The results with those based on Quasi-Crystalline Approximation (QCA) are compared in Section 4. Theoretical results of four Stokes brightness temperature with typical parameters of foam based on Monte Carlo simulations [*Chen et al.*, 2003] in passive remote sensing at 10.8 *GHz*, 19 *GHz* and 36.5 *GHz* are illustrated in Section 5. Four Stokes parameters of emission with various wind speed and their azimuthal variations are studied.

2. Formulation

2.1. Foam Model

[4] We modeled the foam as densely packed spherical air bubbles with thin seawater coating [*Guo et al.*, 2001; *Chen et al.*, 2003]. In dense media theory, we calculate the extinction, absorption and scattering coefficients by considering the collective effects of a large number of N particles in a volume V. The extinction, absorption and scattering coefficients are defined as the extinction, absorption and scattering cross sections per unit volume. The results converge for large N and V. In the present Monte Carlo simulations, the coated particles are arranged with face-centered-cubic (fcc) structure to achieve high density packing. Then, Monte Carlo simu-lations of solutions of Maxwell equations are applied. 7 realizations are used in the calculation.
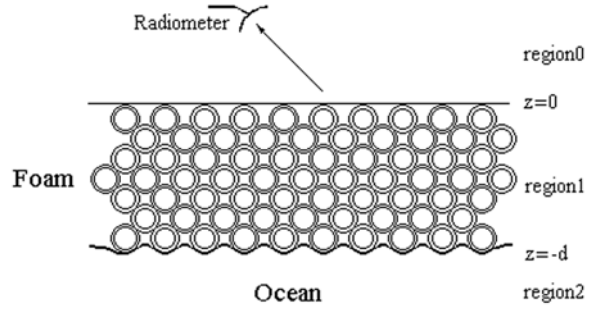

Figure 1. Geometrical configuration for thermal emis-sion from foam-covered rough ocean surface.

[5] Consider one of the six unit-cubic faces, the cubic side length is a, and the diagonal length is $4r$, where r is the sphere radius. Thus the cubic side length a is $2\sqrt{2}r$, and the volume V_c of the unit-cubic is $16\sqrt{2}r^3$. The unit-cubic contains 6 semispheres at the center of each face; and 8 one-eighth-spheres at each zenith. So, all the unit-cubic has 4 spheres. The fraction volume is $\frac{4 \times \frac{4}{3}\pi r^3}{V_c}$, which is equal to $\pi/\sqrt{18}$. Thus, the face-centered-cubic lattice has a fractional volume of $\pi/\sqrt{18} \approx 74\%$ occupied by the particles.

[6] The internal field of each particle can be calculated by using the volume integral equation derived from Maxwell equation [*Tsang et al.*, 2001] for a collection of particles. The extinction coefficient is $\kappa_e = \kappa_s + \kappa_a$ and the Albedo is $\tilde{\omega} = \kappa_s/\kappa_e$. The effective permittivity is calculated as in *Chen et al.* [2003]. The extinction, absorption, scattering coefficients, albedo and effective permittivity are used in DMRT equations. The Rayleigh phase matrix [*Tsang et al.*, 1985, 2000b] is also used.

2.2. Dense Media Radiative Transfer Theory

[7] Consider the thermal emission problem of a foam layer embedded above the wind-generated rough ocean surfaces, as indicated in Figure 1. The foam layer consists of coated dielectric particles in region 1. The DMRT equations for passive remote sensing in region 1 can be written as follows:

$$\frac{d}{dz}\begin{bmatrix} +\overline{I_u}(z,\mu,\phi) \\ -\overline{I_d}(z,\mu,\phi) \end{bmatrix} = -\kappa_{es}\begin{bmatrix} \overline{I_u}(z,\mu,\phi) \\ \overline{I_d}(z,\mu,\phi) \end{bmatrix} + \kappa_{as}C\bar{T}$$
$$+ \begin{bmatrix} \overline{F_u}(z,\mu,\phi) \\ \overline{F_d}(z,\mu,\phi) \end{bmatrix} \quad (1)$$

where $\overline{I_u}$ and $\overline{I_d}$ represent, respectively, upward- and downward-going specific intensities and 4 × 1 column matrices containing the four Stokes parameters; $\mu = \cos\theta$;

$\mu' = \cos\theta'$; $\kappa_{es} = \kappa_e/\cos\theta$; $\kappa_{as} = \kappa_a/\cos\theta$; $\kappa_{ss} = \kappa_s/\cos\theta$; $\overline{T}$ is the temperature profile in the layer.

$$\begin{bmatrix} \overline{F_u}(z,\mu,\phi) \\ \overline{F_d}(z,\mu,\phi) \end{bmatrix} = \frac{\kappa_{ss}}{4\pi} \int_0^1 d\mu' \int_0^{2\pi} d\phi'$$

$$\cdot \begin{bmatrix} \overline{\overline{P}}(\mu,\phi;\mu',\phi') & \overline{\overline{P}}(\mu,\phi;-\mu',\phi') \\ \overline{\overline{P}}(-\mu,\phi;\mu',\phi') & \overline{\overline{P}}(-\mu,\phi;-\mu',\phi') \end{bmatrix}$$

$$\cdot \begin{bmatrix} \overline{I_u}(z,\mu',\phi') \\ \overline{I_d}(z,\mu',\phi') \end{bmatrix} \qquad (2)$$

in which κ_a and κ_s are the absorption and scattering coefficient matrices taken to be diagonal. C is equal to $K_b K'^2/(\lambda^2 k^2)$ and K_b is the Boltzman's constant. $\overline{\overline{P}}(\mu,\phi;\mu',\phi')$ is Rayleigh scattering phase matrix.

2.3. Boundary Conditions

[8] The boundary condition at $z = 0$ is

$$\overline{I_d}(z=0,\theta,\phi) = \overline{\overline{R}}(\theta)\overline{I_u}(z=0,\theta,\phi) \qquad (3)$$

where $\overline{\overline{R}}(\theta)$ is a reflection matrix of the flat surface at the air-foam interface with effective propagation constant K and effective relative permittivity ε_{eff} for dense media.

[9] The rough surface boundary condition at $z = -d$ is bistatic and is determined by second-order SPM.

$$\overline{I_u}(z=-d,\mu,\phi) = \overline{\overline{G_c}}(\mu,\theta)\overline{I_d}(z=-d,\mu,\phi)$$

$$+ \frac{K'^2}{\mu} \int_0^1 d\mu' \int_0^{2\pi} d\phi' \mu'^2 W\big(\overline{k_\perp} - \overline{k'_\perp}\big)$$

$$\cdot \overline{\overline{G_{ic}}}(\mu,\phi;-\mu',\phi')\overline{I_d}(z=-d,\mu',\phi')$$

$$+ \overline{e}CT_g \qquad (4)$$

where $\overline{\overline{G_c}}$ and $\overline{\overline{G_{ic}}}$ are the coherent and incoherent scattering phase matrixes of the rough surface at $z = -d$.

$$\overline{\overline{G_{c,ic}}} = \begin{bmatrix} \langle|f_{vv}|^2\rangle & \langle|f_{vh}|^2\rangle & \mathrm{Re}\langle f_{vv}f_{vh}^*\rangle & -\mathrm{Im}\langle f_{vv}f_{vh}^*\rangle \\ \langle|f_{hv}|^2\rangle & \langle|f_{hh}|^2\rangle & \mathrm{Re}\langle f_{hv}f_{hh}^*\rangle & -\mathrm{Im}\langle f_{hv}f_{hh}^*\rangle \\ 2\mathrm{Re}\langle f_{vv}f_{hv}^*\rangle & 2\mathrm{Re}\langle f_{vh}f_{hh}^*\rangle & \mathrm{Re}\langle f_{vv}f_{hh}^*+f_{vh}f_{hv}^*\rangle & \mathrm{Im}\langle f_{vv}f_{hh}^*-f_{vh}f_{hv}^*\rangle \\ 2\mathrm{Im}\langle f_{vv}f_{hv}^*\rangle & 2\mathrm{Im}\langle f_{vh}f_{hh}^*\rangle & \mathrm{Im}\langle f_{vv}f_{hh}^*+f_{vh}f_{hv}^*\rangle & \mathrm{Re}\langle f_{vv}f_{hh}^*-f_{vh}f_{hv}^*\rangle \end{bmatrix} \qquad (5)$$

For $\overline{\overline{G_c}}$, $f_{\alpha\alpha} = f_{\alpha\alpha}^{(0)} + f_{\alpha\alpha}^{(2)}$, $f_{\alpha\beta} = f_{\alpha\beta}^{(2)}$, and for $\overline{\overline{G_{ic}}}$, $f_{\alpha\beta} = f_{\alpha\beta}^{(1)}$. Here, both of symbols α and β represent v or h. $f_{vv}^{(0)}$ and $f_{hh}^{(0)}$ are Fresnel reflection coefficients for vertical and horizontal polarizations with the zero-order fields considered. $f_{\alpha\beta}^{(1)}$, and $f_{\alpha\beta}^{(2)}$ are scattering

coefficients of the α-polarized component of the first and second-order scattered fields with β-polarized, respectively, which are given in *Tsang and Kong* [2001]. The zero- and second-order fields give the coherent reflection coefficients of the surfaces. $f_{\alpha\beta}^{(1)}$ gives the incoherent polarimetric bistatic scattering coefficient due to the first-order scattered field. They are derived using the second-order small perturbation method (SPM) [*Tsang et al.*, 1985; *Tsang and Kong*, 2001]. T_g is the temperature of the half space below the foam and $\overline{e}$ is the emissivities of the lower boundary.

2.4. Iterative Method of Solution of DMRT Equations With Rough Surface Boundary Conditions

[10] The differential equations (1) have standard solutions of the form

$$\overline{I_u}(z) = \overline{I_u}(-d)e^{-\kappa_{es}(z+d)} + \int_{-d}^z dz'\big[\overline{F_u}(z') + \kappa_{as}C\overline{T}\big]$$

$$\cdot e^{-\kappa_{es}(z-z')} \qquad (6)$$

$$\overline{I_d}(z) = \overline{I_d}(0)e^{\kappa_{es}z} + \int_z^0 dz'\big[\overline{F_d}(z') + \kappa_{as}C\overline{T}\big]e^{\kappa_{es}(z-z')} \qquad (7)$$

Next, we incorporate the rough surface boundary conditions into a form suitable for iterative solutions. Substituting the boundary conditions into (6) and (7), we have

$$\overline{I_u}(z) = e^{-\kappa_{es}(z+d)}\overline{\overline{G_c}}(\mu,\phi)\overline{I_d}(z=-d,\theta,\phi)$$

$$+ e^{-\kappa_{es}(z+d)}\frac{K'^2}{\mu} \int_0^1 d\mu' \int_0^{2\pi} d\phi' \mu'^2 W\big(\overline{k_\perp} - \overline{k'_\perp}\big)$$

$$\cdot \overline{\overline{G_{ic}}}(\mu,\phi;-\mu',\phi')\overline{I_d}(z=-d,\mu',\phi')$$

$$+ \overline{e}CT_g e^{-\kappa_{es}(z+d)} + \int_{-d}^z dz'\big[\overline{F_u}(z') + \kappa_{as}C\overline{T}\big]$$

$$\cdot e^{-\kappa_{es}(z-z')} \qquad (8)$$

$$\overline{I_d}(z) = \overline{\overline{R}}(\theta)\overline{I_u}(z=0,\theta,\phi)e^{\kappa_{es}z} + \int_z^0 dz'\big[\overline{F_d}(z') + \kappa_{as}C\overline{T}\big]$$

$$\cdot e^{\kappa_{es}(z-z')} \qquad (9)$$

[11] The source terms in (8) are the upward temperature originating from the layer temperature profile. The contribution from the lower half space is $\overline{e}CT_g e^{-\kappa_{es}(z+d)}$. The source term in (9) is the downward temperature. All other terms in (8) that depend on the upward and down-

ward temperatures can be evaluated using these three source terms. After taking integration over z, we have

$$
\overline{V}(z=0) = \int_{-d}^{0} dz' \overline{F_u}(z') e^{\kappa_{es} z'} \approx \frac{1}{4\pi} \frac{\kappa_s \kappa_a}{\kappa_e \kappa_e}
$$
$$
\cdot \int_0^1 d\mu' \int_0^{2\pi} d\phi' \overline{\overline{P}}(\mu, \phi; \mu', \phi')
$$
$$
\cdot \left[c_0 \overline{T} + \left(\overline{e} C T_g \frac{\kappa_e}{\kappa_a} - \overline{T} \right) c_1 e^{-\kappa_e d/\mu'} \right]
$$
$$
+ \frac{1}{4\pi} \frac{\kappa_s \kappa_a}{\kappa_e \kappa_e} \int_0^1 d\mu' \int_0^{2\pi} d\phi' \overline{\overline{P}}(\mu, \phi; -\mu', \phi')
$$
$$
\cdot \overline{T}(c_0 - c_2) \tag{10}
$$

where

$$
c_0 = 1 - \exp(-\kappa_{es} d)
$$
$$
c_1 = \{1 - \exp[-\kappa_{es} d(1 - \mu/\mu')]\}/(1 - \mu/\mu')
$$
$$
c_2 = \{1 - \exp[-\kappa_{es} d(1 + \mu/\mu')]\}/(1 + \mu/\mu')
$$

Another term in (8) accounting for upward scattering of the downward temperature by the lower boundary at $z = -d$ can be evaluated as

$$
\overline{S}(z=0) = \overline{\overline{G_c}}(\mu, \phi) \overline{I_d}(z = -d, \theta, \phi) e^{-\kappa_{es} d}
$$
$$
+ \frac{K'^2}{\mu} \int_0^1 d\mu' \int_0^{2\pi} d\phi' \mu'^2 W\left(\overline{k_\perp} - \overline{k'_\perp}\right)
$$
$$
\cdot \overline{\overline{G_{ic}}}(\mu, \phi; -\mu', \phi') \overline{I_d}(z = -d, \mu', \phi') e^{-\kappa_{es} d}
$$
$$
\approx C \frac{\kappa_a}{\kappa_e} \overline{\overline{G_c}}(\mu, \phi) \overline{T}\left(1 - e^{-\kappa_{es} d}\right) e^{-\kappa_{es} d}
$$
$$
+ C \frac{\kappa_a}{\kappa_e} \frac{K'^2}{\mu} \int_0^1 \mu' \int_0^{2\pi} d\phi' \mu'^2 W\left(\overline{k_\perp} - \overline{k'_\perp}\right)
$$
$$
\cdot \overline{\overline{G_{ic}}}(\mu, \phi; -\mu', \phi') \overline{T}\left(1 - e^{-\kappa_e d/\mu'}\right) e^{-\kappa_{es} d}
$$
$$
\tag{11}
$$

Thus the complete expression for the upward temperature at $z = 0$ within the layer is

$$
\overline{I_u}^{(1)}(z=0) = C \frac{\kappa_a}{\kappa_e} \overline{T}\left[1 - e^{-\kappa_{es} d}\right] + \overline{e} C T_g e^{-\kappa_{es} d}
$$
$$
+ \overline{V}(z=0) + \overline{S}(z=0) \tag{12}
$$

This is the first-order solution of $\overline{I_u}$. The second-order solution for the upward temperature at $z = 0$ is

$$
\overline{I_u}^{(2)}(z=0) = C \frac{\kappa_a}{\kappa_e} \overline{T}\left[1 - e^{-\kappa_{es} d}\right] + \overline{e} C T_g e^{-\kappa_{es} d}
$$
$$
+ \overline{V}(z=0) + \overline{S}^{(2)}(z=0) \tag{13}
$$

where

$$
\overline{S}^{(2)}(z=0) = \overline{\overline{G_c}}(\mu, \phi) \overline{I_d}(z = -d, \theta, \phi) e^{-\kappa_{es} d}
$$
$$
+ \frac{K'^2}{\mu} \int_0^1 d\mu' \int_0^{2\pi} d\phi' \mu'^2 W\left(\overline{k_\perp} - \overline{k'_\perp}\right)
$$
$$
\cdot \overline{\overline{G_{ic}}}(\mu, \phi; -\mu', \phi') \overline{I_d}(z = -d, \mu', \phi') e^{-\kappa_{es} d}
$$
$$
\tag{14}
$$

[12] The brightness temperatures $\overline{T_B}$ in the direction (θ_0, ϕ_0), where $\theta_0 = \sin^{-1}(K'\sin\theta/k)$ as related to θ by Snells' law, are given by

$$
\overline{T_B}(\theta_0, \phi_0) = \overline{\overline{T}}(\theta) \overline{I}(z = 0, \theta, \phi) \tag{15}
$$

where $\overline{\overline{T}}$ is given by *Tsang and Kong* [2001, p. 343].

3. FOAM Model Parameters

[13] We assume that there are N_s species of air bubbles with seawater coating embedded in a background of air, as shown in region 1 of Figure 1. The foam parameters are defined as follows: d, foam layer thickness; a_j, outer radius of coated air bubbles of the jth species; b_j, inner radius of coated air bubbles of the jth species; f_j, fractional volume of coated air bubbles of the jth species

$$
f_j = \frac{4\pi}{3} n_{sj} a_j^3
$$

where n_{sj} is the number of the jth species per unit volume. The parameter f is the total fractional volume of air bubbles

$$
f = \sum_{j=1}^{N_s} f_j
$$

and parameter f_w is the fractional volume of seawater in foam

$$
f_w = \sum_{j=1}^{N_s} f_j \left[1 - \left(\frac{b_j}{a_j} \right)^3 \right].
$$

[14] The air region includes the core regions of the coated particles as well as the interstitial space between them. Thus the foam void fractional volume is

$$
f_v = 1.0 - f_w.
$$

By choosing various values for a_j and b_j, f_v can be on the order of 90%, which agrees well with the

Table 1. Parameters of Foam Model for the Simulated Results in Figures 2 and 3

Parameter	Value
d	3 cm
$2a$	2000 μm
$2b_1$	1220 μm
$2b_2$	1995.9 μm
f	74%
f_w	10.3%
f_1	12.9%
f_2	61.1%

experimental measurements of artificially generated foam [*Rose et al.*, 2003]. The experimental measurements were conducted at the Chesapeake Bay Detachment at 10.8 *GHz* and 36.5 *GHz*. The diameters of air bubbles range from 500 μm to 5000 μm with median between 900 μm and 1000 μm. An average foam layer is 2.8 *cm*.

4. Comparison With QCA

[15] In this section, we compare the results with those based on QCA [*Guo et al.*, 2001], in which wave scattering and emission in a medium consisting of densely packed coated particles are solved by using QCA in combination with the dense medium radiative transfer theory.

[16] Using the parameters of foam model in Table 1, the quantities for foam layer calculated by QCA and by Monte Carlo simulations are shown in Tables 2 and 3, respectively. We assume that there are two species of air bubbles, which have the same outer radius a, but have different coating thickness with inner radii of b_1 and b_2. Emissivities of horizontal polarization and vertical polarization are simulated at 10.8 *GHz* and 36.5 *GHz*. Figure 2 is based on Monte Carlo simulations. We can see that the emissivities at 10.8 *GHz* and 36.8 *GHz* are comparable. This feature is consistent with experimental measurements [*Rose et al.*, 2003]. On the other hand, as shown in Figure 3, which is based on QCA, the emissivities at 36.5 *GHz*
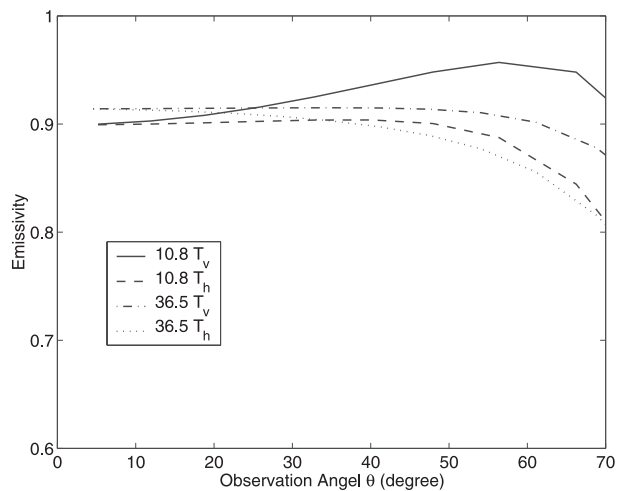
Table 2. Quantities of Foam Based on QCA

Parameter	10.8 *GHz*	36.5 *GHz*
Absorption rate κ_a, cm^{-1}	0.1763	0.8154
Scattering rate κ_s, cm^{-1}	0.0567	0.7299
Extinction rate κ_e, cm^{-1}	0.2330	1.5453
Albedo	0.2435	0.4724
Effective permittivity ε_{eff}	1.4573 + i0.1245	1.2944 + i0.231

Table 3. Quantities of Foam Based on Monte Carlo Simulations

Parameter	10.8 *GHz*	36.5 *GHz*
Absorption rate κ_a, cm^{-1}	0.2990	0.9400
Scattering rate κ_s, cm^{-1}	0.0165	0.6183
Extinction rate κ_e, cm^{-1}	0.3155	1.5583
Albedo	0.0552	0.6578
Effective permittivity ε_{eff}	1.4900 + i0.1700	1.1600 + i0.220

are higher than at 10.8 *GHz*. For dense media consisting of particles densely packed, there are two different cases. They are differentiated by large loss tangent and small loss tangent where loss tangent is $\frac{\sigma}{\omega\varepsilon}$ and σ is the conductivity of the medium. For large loss tangent, it represents the case that conductive current is much larger than displacement current, while the opposite is true for the small loss tangent case. It has been shown by extensive simulations [*Tsang et al.*, 1992] that QCA is valid for the small loss tangent case. The QCA theory has been successful in dry snow [*Tsang et al.*, 2000a]. However, the QCA theory is less successful when conductive current dominates [*Chew et al.*, 1990]. The conductive current can go through several connected particles. On the other hand, QCA is limited to pair distribution functions. Thus the applicability of QCA is also dependent on frequency through the dependence on $\frac{\sigma}{\omega\varepsilon}$. In this paper, we see that the results of QCA are

Figure 2. Emissivities as a function of observation angle for vertical and horizontal polarizations at 10.8 *GHz* and 36.5 *GHz*, using model based on Monte Carlo simulations.
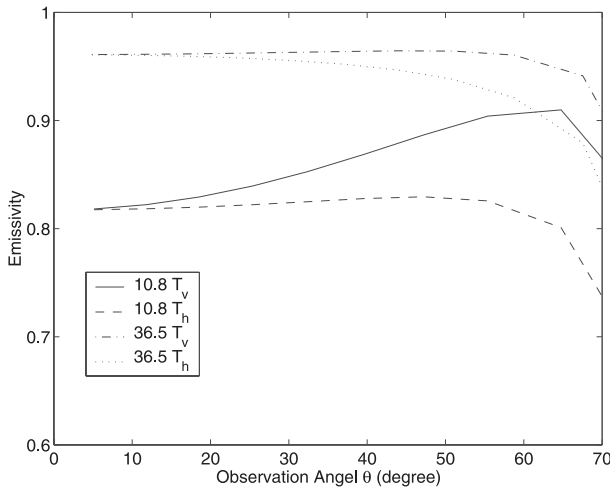
Figure 3. Emissivities as a function of observation angle for vertical and horizontal polarizations at 10.8 *GHz* and 36.5 *GHz*, using model based on QCA.

5. Numerical Illustration of Four Stokes Parameters

[17] The foam model based on Monte Carlo simulations is used to calculate the extinction, absorption and scattering coefficients. The parameters of foam model are listed in Table 4, and the quantities of foam layer are described in Table 5. To describe the wind-induced wave on the ocean surface, the empirical surface spectrum W proposed by *Durden and Vesecky* [1985] was used. The choice of this spectrum is because much of the observed dependence of the radar cross section on frequency, polarization, incidence angle, and wind velocity was predicted by using this spectrum function. There were some typographical errors in *Durden and Vesecky* [1985]. The expressions of the spectrum were corrected in *Yueh et al.* [1994] and listed in Appendix A. In the model, a_0 is the absolute magnitude of the spectrum. Since a parametric analysis has been carried out showing that $a_0 = 0.008$ gives the best agreement with experiment data in *Yueh et al.* [1994], a_0 of 0.008 is used for

Table 4. Parameters for Foam Model

Parameter	Value
d	1 *cm*
$2a$	500 μ*m*
$2b_1$	260 μ*m*
$2b_2$	498.9 μ*m*
f	74%
f_w	10.2%
f_1	11.4%
f_2	62.6%

calculations in this paper. The wave-number cutoff k_d is a key parameter in the spectrum. The quantity, k_d, can be selected to be sufficiently large to satisfy the small perturbation method condition [*Yueh et al.*, 1994; *Yueh*, 1997]. In the following studies, we choose k_d equal to 100 *rad/m* for 10.8 *GHz*, 120 *rad/m* for 19 *GHz* and 230 *rad/m* for 36.5 *GHz*, with kh equal to 0.25, 0.38 and 0.41, respectively. The parameter h is the rms height of small-scale surface. Note that the values of kh are all less than 0.42. As investigated in *Yueh et al.* [1994], the SPM should be applicable to these cases. The permittivity of seawater is calculated from the model of *Klein and Swift* [1977] with the water temperature of 284 K and salinity of 20 per thousand. The permittivities of the seawater at 10.8 *GHz*, 19 *GHz* and 36.5 *GHz* are $49.1493 + i40.1053$, $28.9541 + i36.8340$ and $13.4480 + i24.7844$, respectively.

[18] To demonstrate the effects of the thickness of the foam layer, we plot the brightness temperature of four Stokes as a function of thickness of foam layer in Figure 4. As the thickness of the foam layer increases, the mean values of T_v and T_h will increase correspondingly and then saturate at particular thickness of the foam layer. On the other hand, U and V components will decrease to zero. For horizontal and vertical polarizations, saturation occurs around 7 *cm*, 3 *cm* and 2 *cm* of foam thickness at 10.8 *GHz*, 19 *GHz* and 36.5 *GHz*, respectively. For U and V components, saturation occurs at a larger layer thickness of 14 *cm*, 7 *cm* and 4 *cm*, respectively.

[19] Figure 5 illustrates the Stokes parameters as a function of the zenith angle θ with a fixed azimuth

Table 5. Quantities of Foam Using Monte Carlo Simulations

Parameter	Albedo	Extinction Rate κ_e	Effective Permittivity ε_{eff}
10.8 *GHz*	1.791×10^{-4}	0.2723 *cm^{-1}*	$1.4971 + i0.1475$
19.0 *GHz*	1.763×10^{-3}	0.5363 *cm^{-1}*	$1.446 + i0.1623$
36.5 *GHz*	1.642×10^{-2}	0.9802 *cm^{-1}*	$1.3717 + i0.1504$

in better agreement with those of Monte Carlo simulations at high frequency of 36.5 GHz, and less successful at low frequency of 10.8 GHz. The experiment in *Guo et al.* [2001] was at 19.0 GHz, and QCA was reasonably successful. Since Monte Carlo simulations provide the exact solution of Maxwell equations, this model will be applied to calculate the four Stokes parameters in the following studies.
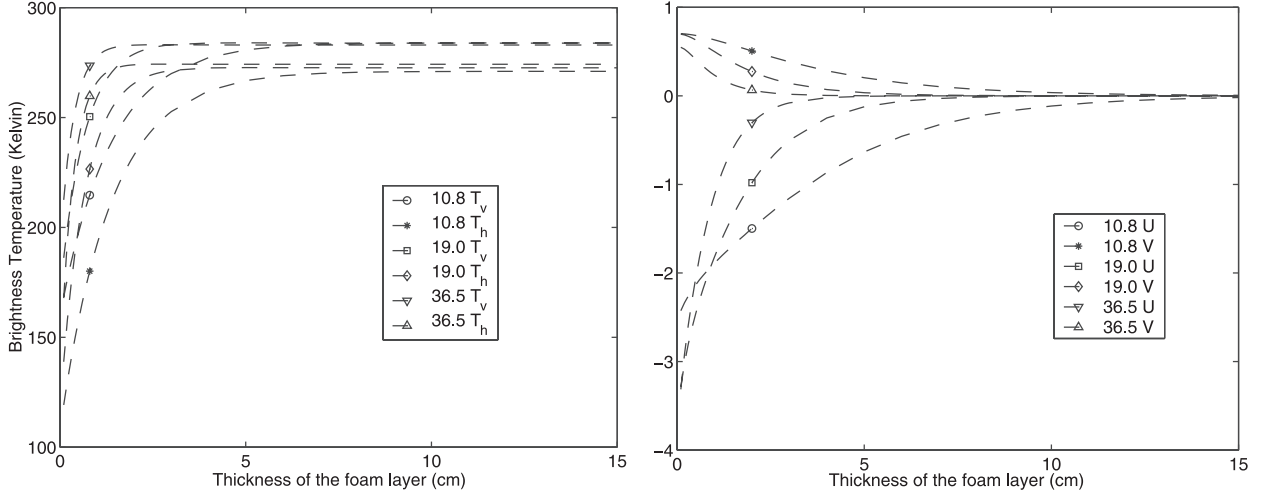
Figure 4. Brightness temperatures as a function of the thickness of the foam layer at aspect angle θ = 53°, at 10.8 *GHz*, 19 *GHz* and 36.5 *GHz*.

angle of ϕ = 45°. We also compare the results of ocean rough surface calculated by SPM. Note that at those frequencies, the mean values of first two Stokes parameters are increased with the presence of foam, and the third and fourth parameters, on the contrary, are reduced. Figure 6 compares the azimuthal variations of four Stokes parameters over a 360° circle for viewing with θ = 30°. It is shown that the Stokes parameters have a cos2ϕ variation in azimuth for T_v and T_h, and sin2ϕ for U and V. That is, T_v and T_h have an even symmetry with respect to the wind direction, while U and V have an odd symmetry. Comparing with the results of SPM, the magnitudes of azimuthal variations become decreased. The level of decrease is bigger as the frequency becomes bigger. T_v and T_h of azimuthal variations are decreased by 0.1 *K* and 0.085 *K* at 10.8 *GHz*; 0.7 *K* and 0.44 *K* at 19 *GHz*; 1.45 *K* and 1.4 *K* at 36.5 *GHz*, respectively. The decrease is caused by attenuation through foam layer. For prediction of values of azimuthal variations, some other effects should be included (such as, tilting effects of large-scale surfaces) which are not considered in this paper.

[20] To demonstrate the contribution of ocean roughness, we compare the results with those of foam-covered smooth ocean surfaces in Figure 7. It can be seen that the brightness temperatures of T_v and T_h are approximately increased by 10*K* at nadir viewing, after considering the effects of rough ocean surfaces.

[21] The four Stokes parameters of brightness temperature are sensitive to wind speeds. In Figures 8−10, the results for foam-covered rough ocean surfaces at

wind speed $U_{19.5}$ = 10 *m/s* are presented and compared with those at $U_{19.5}$ = 20 *m/s*. $U_{19.5}$ is the wind speed at elevation of 19.5 *m*. At lower wind speed, all four Stokes parameters are reduced. The magnitudes of azimuthal variations at 10 *m/s* are approximately half of those at 20 *m/s*.

[22] For partially foam-covered surfaces the emissivity may be written as [*Ulaby et al.*, 1982]

$$e = (1 - F)e_{sw} + Fe_f$$

where F is the fractional foam coverage, e_{sw} is the emissivity of the wind-roughened ocean surface, and e_f is the emissivity of the foam. The Stokes brightness temperatures can be calculated for a given F and using the results of this paper.

6. Conclusions

[23] Four Stokes parameters of brightness temperature for foam-covered rough ocean are theoretically analyzed. Important features are shown by the results at 10.8 *GHz*, 19 *GHz* and 36.5 *GHz* for the four Stokes parameters. These are important to determine how the foam affects the brightness temperatures and the retrieval of the ocean surface wind vector. The first two Stokes parameters are increased with the presence of foam, and the third and fourth parameters are reduced. The azimuthal variations of polarimetric brightness temperature are also illustrated. The first two Stokes parameters are even function of ϕ, while
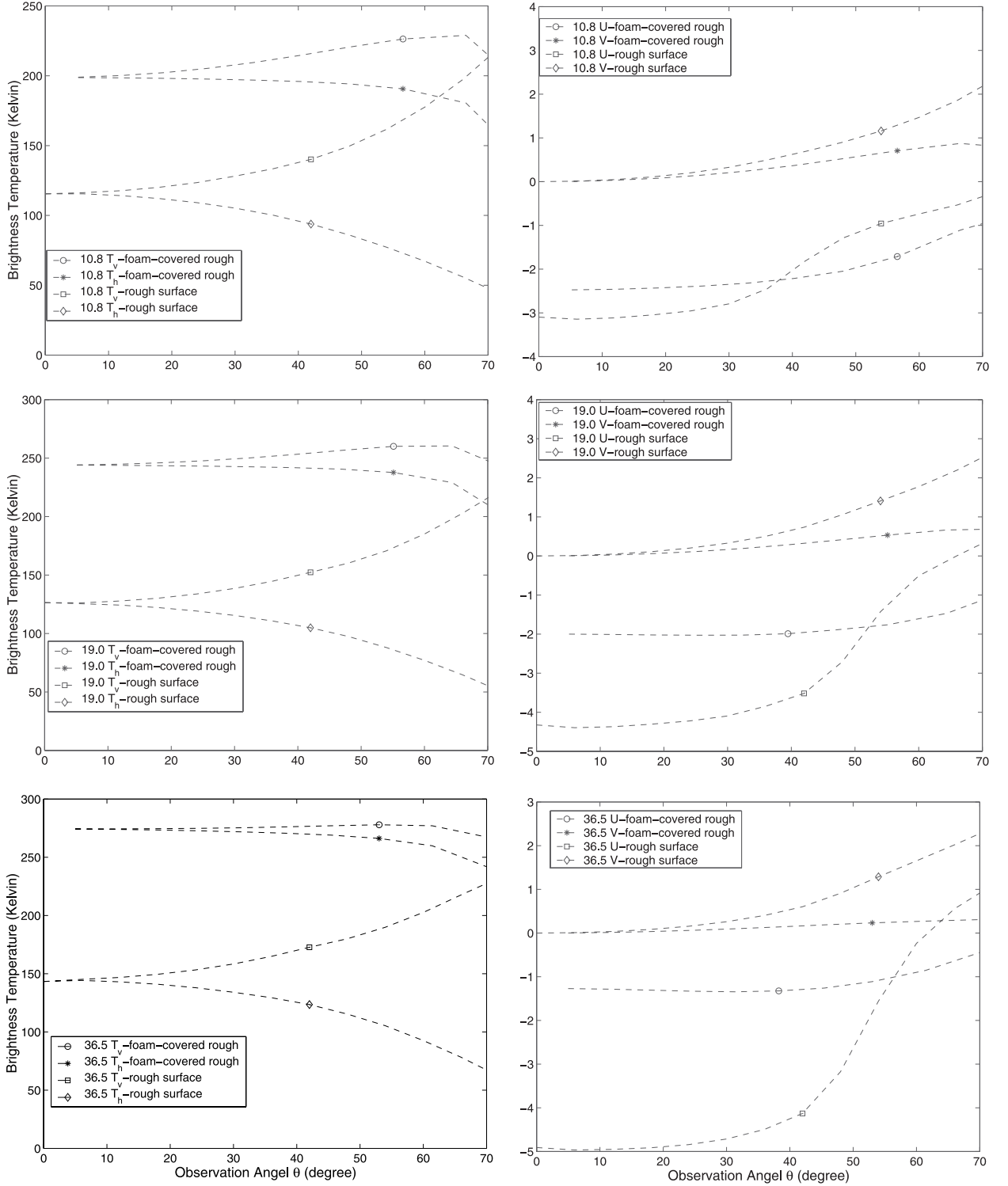
Figure 5. Comparison of four Stokes parameters versus aspect angle θ at 10.8 *GHz*, 19 *GHz* and 36.5 *GHz* for the foam-covered rough ocean surface calculated by the iterative method, and for the rough ocean surface calculated by SPM. Azimuth observation angle ϕ = 45°; wind speed = 20 *m/s*.
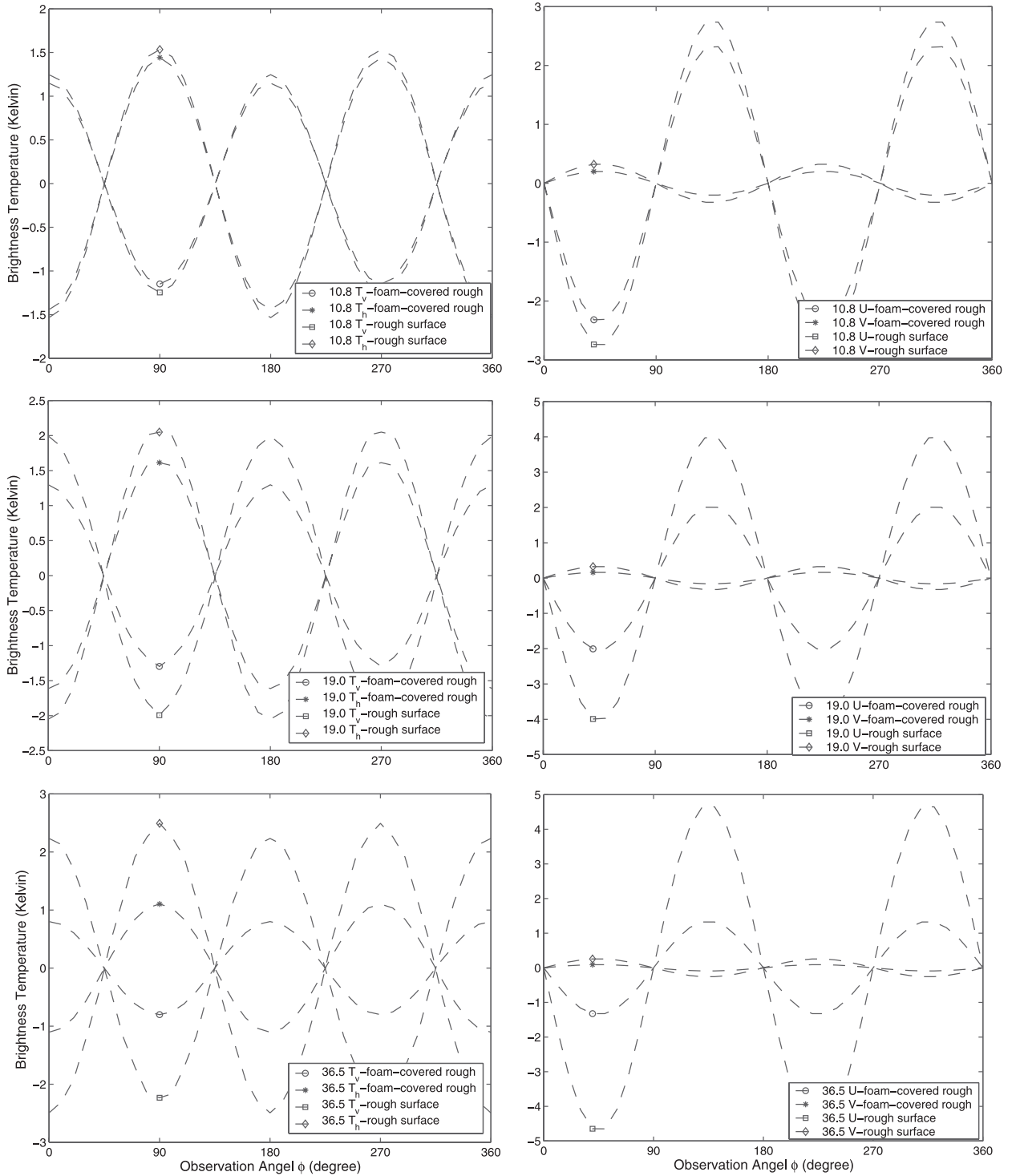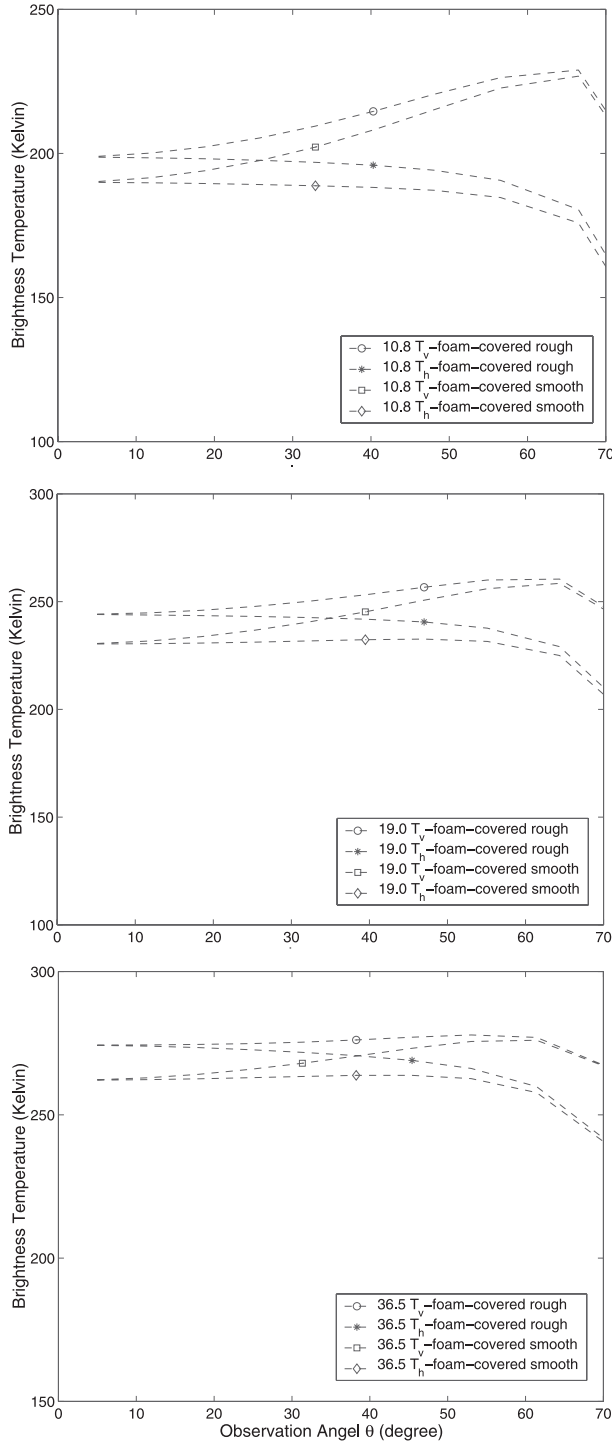
Figure 6. Comparison of four Stokes parameters versus azimuth angle φ at 10.8 *GHz*, 19 *GHz* and 36.5 *GHz* for the foam-covered rough ocean surface calculated by the iterative method, and for the rough ocean surface calculated by SPM. Aspect observation angle θ = 30°; wind speed = 20 *m/s*.

Figure 7. Comparison of brightness temperatures versus aspect angle θ at 10.8 *GHz*, 19 *GHz* and 36.5 *GHz* between the foam-covered rough ocean surface and the foam-covered smooth ocean surface. Azimuth observation angle φ = 45°; wind speed = 20 *m/s*.

the last two parameters are odd functions. Emissions with various wind speeds and foam layer thickness are also studied. The four Stokes parameters of brightness temperature are dependent on wind speeds and foam thickness.

Appendix A: Empirical Sea Surface Spectrum

[24] The surface spectrum proposed by *Durden and Vesecky* [1985] for $k > k_j = 2$ is given as

$$W(k, \phi) = \frac{1}{2\pi k} S(k) \Phi(k, \phi), \qquad (A1)$$

where

$$S(k_\rho) = \frac{a_0}{k^3} \left(\frac{bku_*^2}{g_*} \right)^{a \log_{10} \left(\frac{k}{K_j} \right)} \qquad (A2)$$

$$\Phi(k, \phi) = 1 + c\left(1 - e^{-sk^2}\right) \cos 2\phi.$$

Here $g_* = g + \gamma k^2$ with $\gamma = 7.25 \times 10^{-5}$, $a = 0.225$, $b = 1.25$, and $g = 9.81$. The value of a_0 represents the absolute magnitude of the spectrum.

[25] The wind speed given at any elevation z can be calculated from u_* by $U(z) = \frac{u_*}{0.4} \log(\frac{z}{Z_0})$. u_* is related to Z_0 by

$$Z_0 = 0.0000684/u_* + 0.00428u_*^2 - 0.000443.$$

The coefficients of the angular part of the spectrum are

$$c = \left(\frac{1 - R}{1 + R} \right) \frac{2}{1 - D}$$

$$R = \frac{0.003 + 0.00192U(12.5)}{0.00316U(12.5)}$$

$$D = \frac{\int_0^\infty k^2 S(k) e^{-sk^2} dk}{\int_0^\infty k^2 S(k) dk}.$$
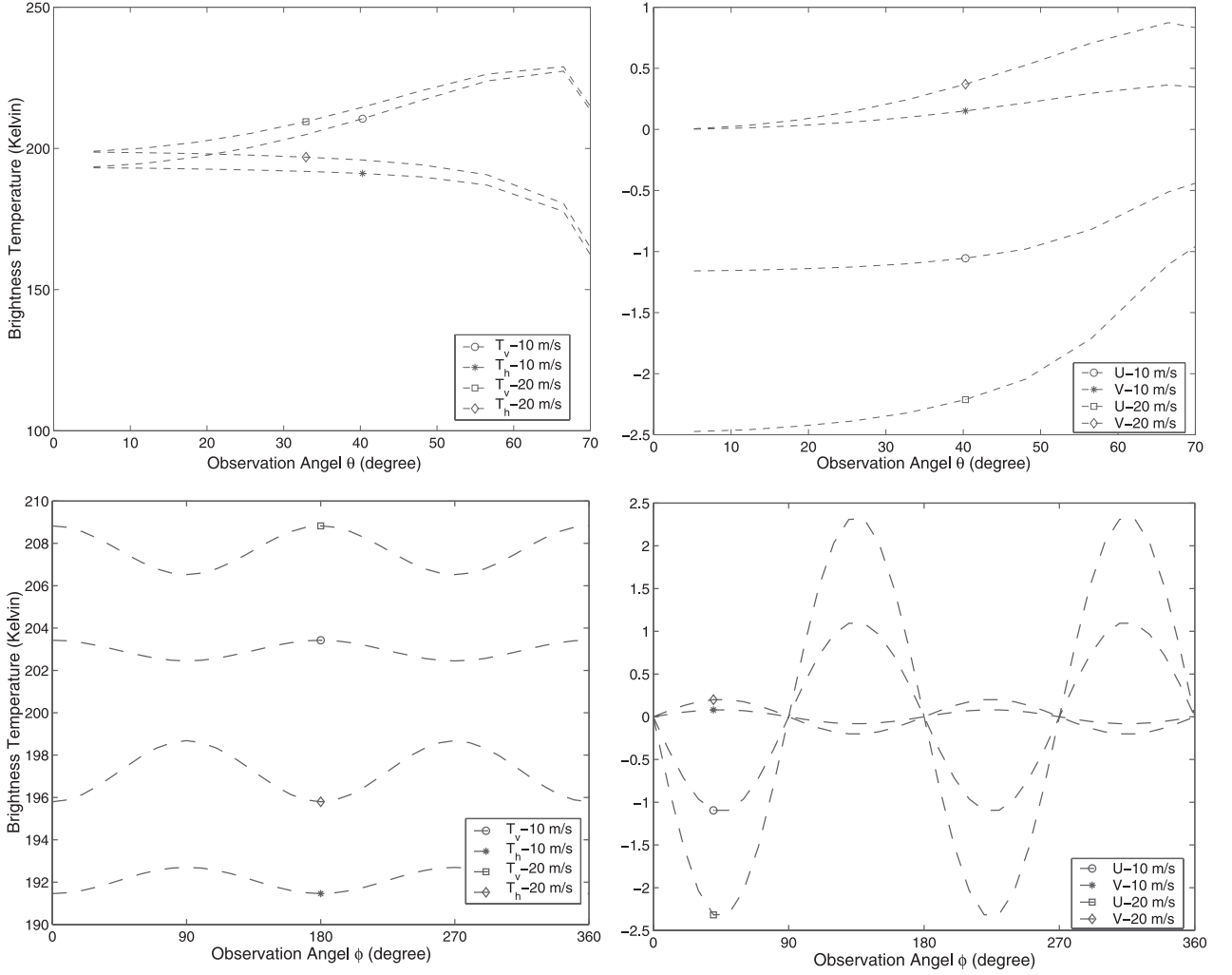
Figure 8. Wind speed dependence at 10.8 *GHz* versus aspect angle θ at a fixed ϕ = 45° and versus azimuth angle ϕ at a fixed θ = 30°.
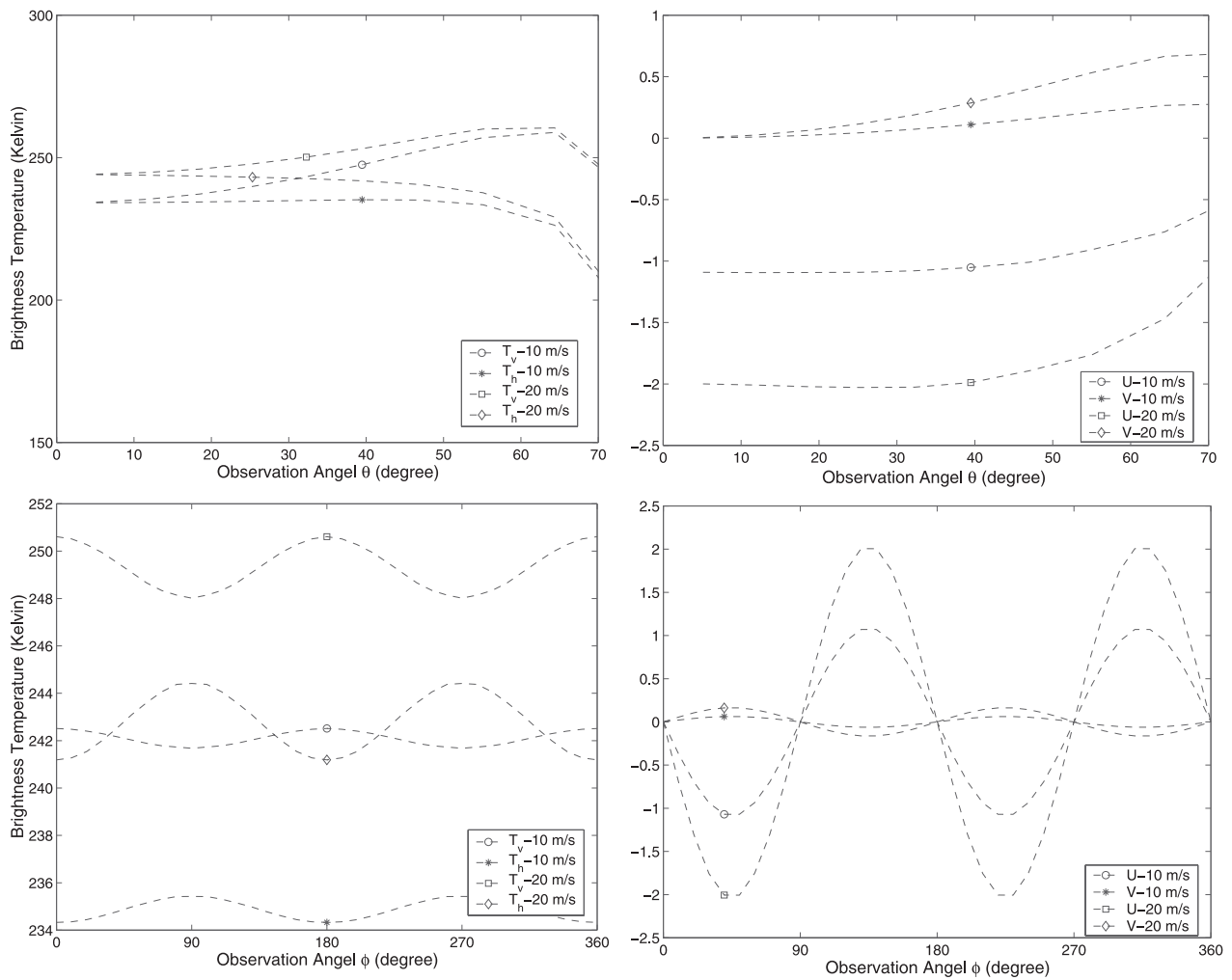
Figure 9. Wind speed dependence at 19.0 *GHz* versus aspect angle θ at a fixed φ = 45° and versus azimuth angle φ at a fixed θ = 30°.

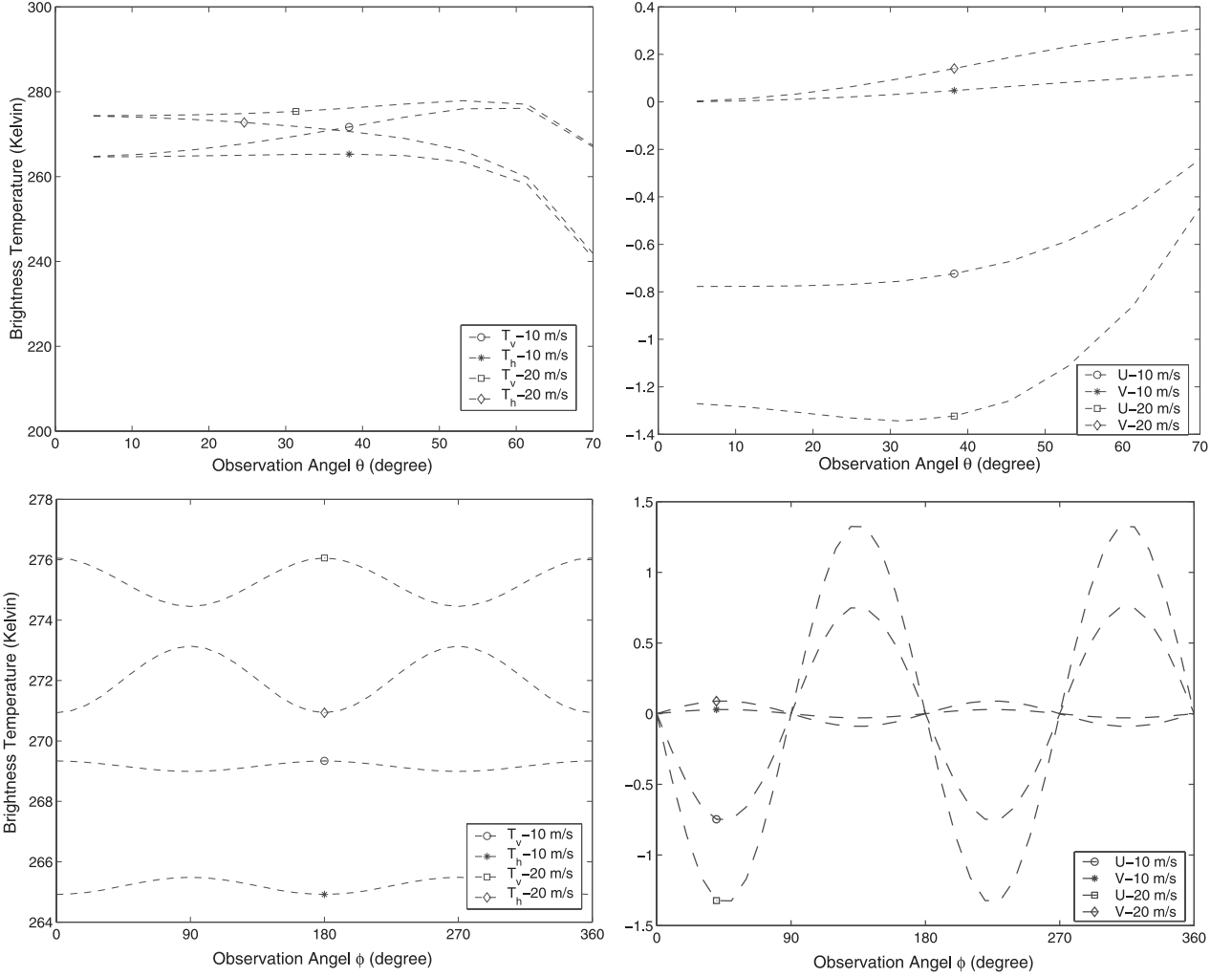**Figure 10.** Wind speed dependence at 36.5 *GHz* versus aspect angle θ at a fixed φ = 45° and versus azimuth angle φ at a fixed θ = 30°.

References

Chen, D., L. Tsang, L. Zhou, S. C. Reising, W. Asher, L. A. Rose, K. St. Germain, K. H. Ding, and C. T. Chen, Microwave emission and scattering of foam based on Monte Carlo simulations of dense media, *IEEE Trans. Geosci. Remote Sens.*, *41*, 782–790, 2003.

Chew, W. C., J. A. Friedrich, and R. Geiger, A multiple scattering solution for the effective permittivity of a sphere mixture, *IEEE Trans. Geosci. Remote Sens.*, *28*(2), 207–214, 1990.

Durden, S. P., and J. F. Vesecky, A physcial radar cross section model for a wind driven sea with swell, *IEEE J. Oceanic Eng.*, *10*, 445–451, 1985.

Guo, J., L. Tsang, W. Asher, K. H. Ding, and C. T. Chen, Applications of dense media radiative transfer theory for passive microwave remote sensing of foam covered ocean, *IEEE Trans. Geosci. Remote Sens.*, *39*(5), 1019–1027, 2001.

Huang, X. Z., and Y. Q. Jin, Scattering and emission from two-scale randomly rough sea surface with foam scatterers, *IEE, Part H*, *142*(2), 109–114, 1995.

Johnson, J. T., J. A. Kong, R. T. Shin, S. H. Yueh, S. V. Nghiem, and R. Kwok, Polarimetric thermal emission from rough ocean surfaces, *J. Electromagn. Waves Appl.*, *8*(1), 43–59, 1994.

Klein, L. A., and C. T. Swift, An improved model for the dielectric constant of seawater at microwave frequencies, *IEEE Trans. Antennas Propag.*, *25*(1), 104–111, 1977.

Kunkee, D. B., and A. J. Gasiewski, Simulation of passive microwave wind direction signatures over the ocean using an asymmetric-wave geometrical optics model, *Radio Sci.*, *32*, 59–78, 1997.

Pandey, P. C., and R. K. Kakar, An empirical microwave emissivity model for a foam-covered sea, *IEEE J. Oceanic Eng.*, *7*(3), 135–140, 1982.

Rose, L. A., W. Asher, S. C. Reising, P. W. Gaiser, K. M. St. Germain, D. J. Dowgiallo, K. A. Horgan, G. Farquharson, and E. J. Knapp, Radiometric measurements of the microwave emissivity of foam, *IEEE Trans. Geosci. Remote Sens*, in press, 2003.

Smith, P. M., The emissivity of sea foam at 19 and 37 GHz, *IEEE Trans. Geosci. Remote Sens.*, *26*, 541–547, 1988.

Stogryn, A., Emissivity of sea foam at microwave frequencies, *J. Geophys. Res.*, *77*, 1658–1666, 1972.

Tsang, L., Polarimetric passive microwave remote sensing of random discrete scatterers and rough surfaces, *J. Electromagn. Waves Appl.*, *5*(1), 41–57, 1991.

Tsang, L., and J. A. Kong, *Scattering of Electromagnetic Waves*, vol. 3, *Advanced Topics*, Wiley-Interscience, Hoboken, N. J., 2001.

Tsang, L., J. A. Kong, and R. Shin, *Theory of Microwave Remote Sensing*, Wiley-Interscience, Hoboken, N. J., 1985.

Tsang, L., C. E. Mandt, and K. H. Ding, Monte Carlo simulations of the extinction rate of dense media with randomly distributed dielectric spheres based on solution of Maxwell's equations, *Opt. Lett.*, *17*(5), 314–316, 1992.

Tsang, L., C. T. Chen, A. T. C. Chang, J. Guo, and K. H. Ding, Dense media radiative transfer theory based on quasicrystalline approximation with application to passive microwave remote sensing of snow, *Radio Sci.*, *35*, 731–749, 2000a.

Tsang, L., J. A. Kong, and K. H. Ding, *Scattering of Electromagnetic Waves*, vol. 1, *Theories and Applications*, Wiley-Interscience, Hoboken, N. J., 2000b.

Tsang, L., J. A. Kong, K. H. Ding, and C. O. Ao, *Scattering of Electromagnetic Waves*, vol. 2, *Numerical Simulations*, Wiley-Interscience, Hoboken, N. J., 2001.

Ulaby, F. T., R. K. Moore, and A. K. Fung, *Microwave Remote Sensing: Active and Passive*, Addison-Wesley-Longman, Reading, Mass., 1982.

Wilheit, T. T., Jr., A model for the microwave emissivity of the ocean's surface as a function of wind speed, *IEEE Trans. Geosci. Electron.*, *17*, 244–249, 1979.

Williams, G. F., Microwave emissivity measurements of bubbles and foam, *IEEE Trans. Geosci. Electron.*, *9*, 221–224, 1971.

Yueh, S. H., Modeling of wind direction signals in polarimetric sea surface brightness temperatures, *IEEE Trans. Geosci. Remote Sens.*, *35*, 1400–1418, 1997.

Yueh, S. H., R. Kwok, F. K. Li, S. V. Nghiem, W. J. Wilson, and J. A. Kong, Polarimetric passive remote sensing of ocean wind vectors, *Radio Sci.*, *29*(4), 799–814, 1994.

─────────

D. Chen, Department of Electronic Engineering, City University of Hong Kong, 83 Tat Chee Ave., Kowloon, Hong Kong.

L. Tsang and L. Zhou, Department of Electrical Engineering, University of Washington, Box 352500, Seattle, WA 98195, USA. (lzhou@ee.washington.edu)